Surface & Coatings Technology 353 (2018) 355–363

Contents lists available at ScienceDirect

Surface & Coatings Technology

journal homepage: www.elsevier.com/locate/surfcoat

Investigation of microstructure and properties of magnetron sputtered Zr-Si-N thin films with different Si content

P.C. Silva Neto[a], F.G.R. Freitas[a], D.A.R. Fernandez[a], R.G. Carvalho[a], L.C. Felix[a], A.R. Terto[a], R. Hubler[b], F.M.T. Mendes[c], A.H. Silva Junior[d], E.K. Tentardini[a,*]

[a] Universidade Federal de Sergipe, São Cristóvão, SE 49100-000, Brazil
[b] Pontifícia Universidade Católica do Rio Grande do Sul – PUC-RS, Av. Ipiranga, 6681 Porto Alegre, RS, Brazil
[c] Instituto Nacional de Tecnologia, Av. Venezuela, 82, Rio de Janeiro, RJ, Brazil
[d] Universidade Federal do Rio Grande do Sul – UFRGS, Av. Paulo Gama, 110, Porto Alegre, RS, Brazil

ARTICLE INFO

Keywords:
Magnetron sputtering
Thin films
Zr-Si-N
XPS analysis
Oxidation
Nanohardness

ABSTRACT

Zr-Si-N thin films with varying silicon content were deposited by reactive magnetron sputtering in order to investigate the effect of Si content in microstructure, morphology, mechanical properties and oxidation resistance of the coatings. Characterizations were carried out using RBS, GAXRD, XPS, nanohardness, SEM and oxidation tests. Silicon content was set between 0 and 15 at.%. GAXRD results indicate peak intensity reduction and broadening increase due silicon nitride segregation, which is responsible for grain size reduction, reaching magnitudes lower than 10 nm, calculated by Scherrer. XPS confirmed the presence of compounds like ZrN and Si_3N_4. ZrN film is almost fully oxidized at 773 K, while films with high silicon content maintain ZrN grains stable at 973 K. Silicon addition to ZrN provided an increment in hardness values of 32% and also increased H^3/E^2 ratio.

1. Introduction

Transition metal nitride thin films, denominated MeN, where Me represents the elements Ti, Zr, Hf, V, Nb, Ta or Cr, possess a set of valuable properties to industrial applications, such as: high hardness, mechanical and wear resistance, thermal stability, high melting point and chemical inertness. Special attention has been given to titanium nitride (TiN), due to its high hardness and excellent tribological properties, along with chromium and zirconium nitrides, due to their corrosion and oxidation resistance derived from the formation of a protective oxide layer. Such films are frequently deposited on cutting tools aiming to improve their lifespan and provide increased productivity to machining industries [1].

Despite their excellent properties, columnar microstructure and presence of defects such as micro-cracks and porosity, characteristic features of thin films deposited by reactive magnetron sputtering (RMS), limit the field of application for MeN films. Such defects allow the direct contact between external environment and substrate, compromising the application of those coatings in high temperature situations and in the presence of aggressive fluids, which require oxidation and corrosion resistance [2–11].

Additionally, it is important to note that mechanical properties of MeN thin films are associated with a complex state of crystal lattice compression, or residual stress. Thin films deposition process commonly occurs in low temperatures ($T < 570$ K), in which atoms and molecules do not possess sufficient energy to relocate into their equilibrium state. Hence, the resulting film has its structure in a metastable phase, which tends to stabilize into a lower energy state in case necessary activation energy is provided, meaning that the excellent properties of MeN films tend to decline as a function of time and temperature [1,7,12–16].

A well-studied alternative to solve those aspects is the use of ternary systems, such as Me-Si-N, to improve characteristics of MeN coatings. Even in low quantities, the addition of a third element, in this case silicon, is able to alter chemical bonds, structure and morphology of films, consequently modifying their macroscopic properties [1,7,12–23].

Silicon addition to MeN thin films favors the formation of a biphasic microstructure, one crystalline (MeN) and the other amorphous (Si_3N_4). Amorphous phase is formed in the grain boundaries of crystalline phase, promoting a grain size reduction and resulting in a set of similar or even superior properties to those of films discussed so far.

* Corresponding author at: Universidade Federal de Sergipe, Av. Marechal Rondon, S/N, Departamento de Ciência e Engenharia de Materiais, São Cristóvão, SE, Brazil.
E-mail address: etentardini@gmail.com (E.K. Tentardini).

https://doi.org/10.1016/j.surfcoat.2018.07.106
Received 23 April 2018; Received in revised form 1 July 2018; Accepted 12 July 2018
Available online 06 September 2018
0257-8972/ © 2018 Published by Elsevier B.V.

Microstructure, when ideally formed, is composed of grains or crystallites with reduced sizes, embedded by a thin amorphous layer of silicon nitride (Si_3N_4) segregated in grain boundaries [1,12–25]. Thus, the addition of silicon in these films causes them to move from a predominantly columnar structure to a nanocomposite one, formed by transition metal nitride nanocrystals (nc-MeN) embedded in an amorphous phase of silicon nitride (a- Si_3N_4) which improves properties of the material, such as hardness and thermal stability [26–29].

The great advantage of this type of microstructure is its permanence in equilibrium state, not being significantly affected by diffusion activated processes due to its elevated thermal stability [1,11–23]. Furthermore, formation of a nanostructure also improves other properties such as oxidation resistance. Si_3N_4 is a material that possesses great thermal stability and the fact that it involves MeN grains results in a restriction to the diffusion of oxygen inside the film, consequently enhancing oxidation resistance. Raising Si content contributes to increase the thickness of amorphous layer that separates nanograins and the potentiality of films becoming more oxidation resistant.

Particularly, zirconium nitride (ZrN) possesses a distinct oxidation resistance, where zirconium oxide (ZrO_2) formation on the surface has a similar effect of restraining oxygen diffusion to grains inside the film. Nevertheless, oxidation resistance in those films does not surpass 873 K [27,30]. Silicon addition to ZrN thin films is an interesting technical alternative to increase its oxidation resistance.

Although many reports in the literature demonstrate the advantages of silicon addition in MeN thin films [1,12–22,24,31], there are gaps and divergences regarding the formation mechanism of microstructure in Me-Si-N thin films, as well as the influence of Si content and deposition parameters over the physical and chemical properties of the coatings. That is due the constant development in the area, thus new ongoing studies try to explain the phenomena associated with obtaining coatings with enhanced properties against oxidation, corrosion and wear.

This work reports on the influence of silicon addition (0 to 15 at.%) of Zr-Si-N thin films. Those coatings were characterized by RBS, GAXRD, SEM, XPS, nanohardness and oxidation tests.

2. Material and methods

Zr-Si-N thin films were co-deposited by reactive magnetron sputtering with an AJA Orion 5-HV Sputtering Systems model using two individual targets, zirconium and silicon, with 99.97% and 99.99% purity, connected to a DC and RF power supply, respectively. A rotatory sample holder was located at 120 mm of distance between targets and substrate. A summary of main sputtering deposition parameters and material characteristics utilized in the experiments is listed in Table 1.

All deposition parameters were maintained constant during depositions except the power applied in silicon target, which was set at six values: 25W, 50W, 75W, 100W, 125W e 150 W.

Silicon wafer and polyethylene (PE) were employed as substrates. The films deposited on silicon wafer substrate were characterized by Grazing Angle X-ray Diffraction (GAXRD), non-monochromated X-ray Photoelectron Spectroscopy (XPS), nanohardness and oxidation tests, whereas the films deposited on PE were analyzed by Rutherford Backscattering Spectrometry (RBS).

Samples undergone ultrasonic bath in acetone for 30 min. Additionally, immediately before being placed in deposition chamber, Si substrates were cleaned with hydrofluoric acid to remove native SiO_2 layer.

Table 1
Main deposition parameters.

Power to Zr target	120 W
Power to Si target	25 to 100 W
Ar flow rate	19 sccm
N_2 flow rate	2 sccm
Base pressure	1×10^{-6} Pa
Work pressure	4×10^{-1} Pa

RBS at 2.0 MeV was performed with α particle on a 3 MV Tandetron equipment. The analysis was made by a silicon detector positioned at 165° of incident beam and 12 keV resolution in the tests.

Microstructure of the films were analyzed by GAXRD with Shimadzu LabX XRD-6000 instrument, using Cu K_α radiation (40 kV and 30 mA) of 0.154 nm wavelength at an incident angle of 5° and a step size of 0.02° and 2°/min scan speed. Measurement values were obtained at 2Θ from 24° to 60° and peaks were identified by comparison with International Centre for Diffraction Data (ICSD) data files. The XRD data was used to calculate crystallite size by Scherrer, preferential orientation with Harris method [32,33], volumetric fraction of silicon and surface coverage [18].

X-ray photoelectron spectra (XPS) were recorded using a hemispherical spectrometer PHOIBOS 150- SPECS, equipped with X-ray Gun (XR-50) with an Al Kα source (soft X-ray source at 1486.6 eV, which is non-monochromatic). The base pressure in the analysis chamber was about 10^{-8} Pa. The anode was operated at 10 W (10 kV, 10 mA) and the analyzer was operated at a constant pass energy of 50 eV for survey spectra and 20 eV for selected regions. Before analyzes, all samples were subjected to surface cleaning with Ar^+ (1.0 KeV) sputtering procedure for ten minutes. The ion source IQE12/38 from SPECS was used, which allows the operation at 5 KeV beam energy. The incidence angle is preselected to be 50°, as the sample was not tilted (rotation angle at 0°). The binding energy shifts due to surface charging were corrected using the C 1s level at 284.6 eV, as an internal standard. All spectra were performed twice and C 1 s position was measured at the beginning and at the end of each experiment. The spectra were Shirley background-subtracted across the energy region and fitted using CasaXPS Version 2.3.15.

Nanohardness and modulus of elasticity values of the coatings were measured using a IHT Fisherscope HV 100 equipped with a Berkovich diamond indenter. A dynamic load-unload cycle, with load graduated increase and decrease, was applied for 40 s in each sample. The following parameters were standardized in the analysis: use of a 40 nm maximum indentation depth load cycle; cycles run at intervals of 40 s loaded to minimize the effects of the experiment in terms of viscoelastic deformation of the samples; 40 s unloaded (from 40 nm to zero). The load curves were used to calculate the film hardness and the unload curve and the corresponding deflection were recorded and used to calculate the elastic modulus using Oliver and Pharr method. A detailed explanation about these calculations can be obtained elsewhere [34]. For each sample, seven points were measured and the average hardness and standard deviation were obtained.

Scanning Electron Microscope (SEM) analyses were realized on a JEOL JCM 5700. Oxidation tests were performed by muffle oven for 30 min at 773 K, 873 K, 973 K and 1073 K, with heat rate of 10 K/min. The test temperatures were selected so that it can estimate those where decomposition of nitrogen and oxidation reaction processes begin. After oxidation tests the films were analyzed by GAXRD to identify in which temperature the oxidation products peaks occur and SEM in order to observe the surface morphology. Similar procedure was reported previously by other researchers [35–37].

3. Results and discussion

Golden metallic color, characteristic for stoichiometric ZrN thin films [12,26,38,39], was achieved for deposited films. Zr-Si-N reflected different shades of grey, depending of silicon content.

3.1. RBS

All films deposited on polyethylene were analyzed by RBS aiming to determine chemical composition of the coatings and resulting graphs

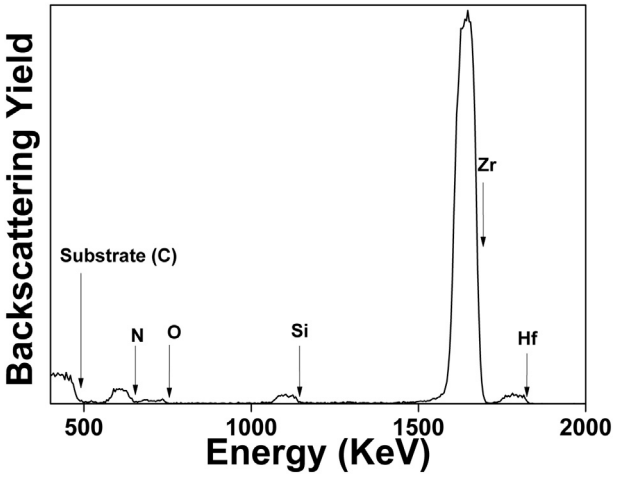

Fig. 1. RBS analysis of $Zr_{0.49}Si_{0.10}N_{0.41}$ coating.

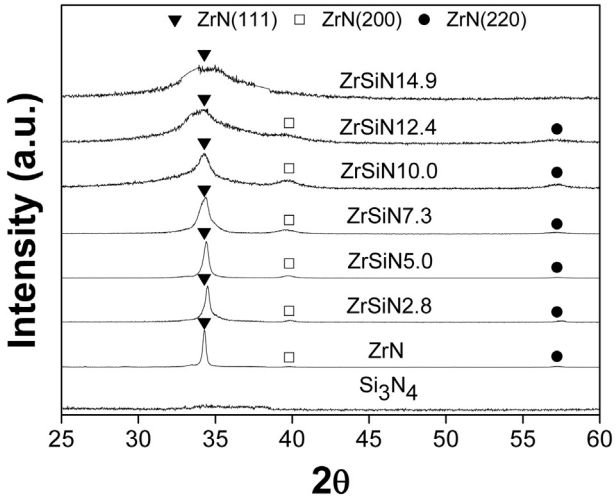

Fig. 2. GAXRD patterns of ZrN, Si_3N_4 and Zr-Si-N samples.

were treated using software RUMP. A typical RBS spectrum is shown in Fig. 1, as obtained from coating $Zr_{0.49}Si_{0.10}N_{0.41}$. The polyethylene substrate was used for RBS analyses to eliminate the high background signal from Si, employed for the other characterizations in this work. Similar spectra (not shown) were obtained for the other Zr-Si-N samples.

Besides peaks related to carbon from the substrate and zirconium, silicon and nitrogen from the thin films, peaks associated to oxygen and hafnium (Hf) can be identified. Oxygen is present at concentrations lower than 3 at.% in the coating and 6 at.% in the interfaces and is derived from residual O_2 and H_2O in deposition chamber. Such contamination is considered unavoidable [40,41] in nitride thin films deposited by RMS. It is known that low levels of oxygen do not cause the formation of oxides during deposition, but substitutes nitrogen in ZrN lattice. Thus, the formation of new chemical compounds and modification of ZrN crystal structure do not occur in those cases [42]. On the other hand, some reports state that the presence of oxygen difficult Si segregation to grain boundaries, preventing the formation of a biphasic structure composed by transition metal nitride crystals embedded by Si_3N_4 [41]. Hafnium is an impurity inherent to Zr target. Table 2 shows chemical composition in terms of Zr, Si and N for all samples, as well as the coatings thicknesses and nomenclature, obtained by RBS analysis. In this table inherent oxygen and hafnium contaminations were disregarded and all nomenclatures are correspondent to zirconium, silicon and nitrogen concentrations.

Coatings deposited for RBS analysis were thinner (~50–90 nm) than those deposited for GAXRD, XPS, SEM, nanohardness and oxidation tests (~600 nm), once RBS technique is more sensitive to separate peaks from chemical elements with similar kinematic factor in coatings possessing thickness inferior to 100 nm.

It is noticeable that Zr-Si-N thin films with lower Si content (ZrSiN2.8, ZrSiN5.0 and ZrSiN7.3) are slightly rich in nitrogen, whereas other samples with higher Si content (ZrSiN10.0, ZrSiN12.4 and ZrSiN14.9) are apparently deficient in nitrogen concentration and that behavior is emphasized with the increase of Si content. Such fact can also be seen in pure Si_3N_4 sample.

Table 2
RBS results showing the composition and thickness of the deposited films on polyethylene in the eight compositions studied. In all samples, oxygen concentration was lower than 3 at.% and was disregarded in the quantification.

Sample	N (at.%)	Si (at.%)	Zr (at.%)	Thickness (nm)
ZrN	50.1 ± 0.6	–	49.9 ± 0.6	57 ± 6
Si_3N_4	51.2 ± 0.6	48.8 ± 0.6	–	62 ± 6
ZrSiN2.8	50.7 ± 0.6	2.8 ± 0.1	46.6 ± 0.6	63 ± 6
ZrSiN5.0	51.0 ± 0.7	5.0 ± 0.1	44.1 ± 0.7	69 ± 7
ZrSiN7.3	51.4 ± 0.7	7.3 ± 0.1	41.3 ± 0.7	73 ± 7
ZrSiN10.0	48.7 ± 0.8	10.0 ± 0.2	41.3 ± 0.8	80 ± 8
ZrSiN12.4	46.4 ± 0.8	12.4 ± 0.2	41.1 ± 0.8	82 ± 8
ZrSiN14.9	44.2 ± 0.8	14.9 ± 0.2	40.9 ± 0.8	84 ± 8

3.2. GAXRD

Fig. 2 shows GAXRD patterns of all samples. It can be noticed in sample ZrN the presence of three diffraction peaks related to crystallographic planes (111), (200) and (220), characteristic for zirconium nitride. Silicon containing phases cannot be detected in Zr-Si-N patterns, similar to sample Si_3N_4. Thus, silicon is presumably forming amorphous compounds or a substitutional solid solution in ZrN lattice, where Si substitutes Zr atoms.

Zr-Si-N films feature all peaks related to ZrN, however, with the increase of Si content it is observed loss of intensity and broadening of those peaks. Sample ZrSiN14.9, which contains 14.9 at.% of Si, is predominantly amorphous.

It is clear, therefore, that Si addition gradually promotes the transition from a crystal structure to an amorphous one. That effect can be explained by the increase of nucleation rate of ZrN grains due to Si incorporation, resulting in a structure formed by crystallite sizes progressively small, as showed in Table 3.

Films with higher Si content showed crystallite sizes inferior to 10 nm. In that situation, the growth of grains is considerably limited, since Si_3N_4 embed ZrN grains, also inhibiting their coalescence and ensuring the formation of nc-ZrN/a-Si_3N_4 nanostructure. There is a limit, where silicon nitride volumetric fraction is so elevated that zirconium nitride molecules cannot be organized to form grains, promoting the formation of an amorphous film, as seen in sample ZrSiN14.9.

From preferential orientation index in Table 3 it is possible to observe a strong preferential orientation in (111) plane for pure ZrN, since the 2.6 value indicate that registered intensity for this peak is 2.6 times greater than expected according to standard diffraction data sheet.

Such fact typically occurs in transition metal nitrides and it is associated with induced defects, such as micro cracks and porosity, inherent from deposition process [43,44], given that is the plane which provides the best accommodation for those defects, reducing deformation energy in the crystal lattice. However, it is noted a reduction in preferential orientation index for plane (111) and an increase of that index for plane (200), which indicates that silicon addition favors the latter crystal orientation. Plane (200) cannot be identified in sample ZrSiN12.4, thus preferential orientation index could not be measured.

Based on XRD data, it can also be inferred that Si solubility limit in

Table 3
Preferential orientation index determined by Harris method, crystallite size calculated by Sherrer method for plane (111), and the volumetric fraction and coverage surface of Si_3N_4 calculated from the XRD data.

Sample	Crystallite size(nm)	Preferential orientation index		Si_3N_4 volumetric fraction(%)	Si_3N_4 coverage surface
		(111)	(200)		
ZrN	36 ± 3	2.6	0.1	–	–
ZrSiN2.8	24 ± 2	2.4	0.2	15.5 ± 0.5	0.26
ZrSiN5.0	21 ± 1	2.5	0.3	25.7 ± 0.4	0.97 ± 0.05
ZrSiN7.3	11 ± 1	2.2	0.4	35.0 ± 0.4	0.95 ± 0.03
ZrSiN10.0	7 ± 1	1.4	0.7	44.4 ± 0.6	0.90 ± 0.04
ZrSiN12.4	3 ± 1	–	–	51.6 ± 0.6	0.52 ± 0.02
ZrSiN14.9	Amorphous	Amorphous	Amorphous	58.3 ± 0.5	Amorphous

ZrN lattice correspond to a concentration below that of sample ZrSiN2.8 (2.8 at.% of Si), since loss of intensity and broadening of peaks can be observed when compared to pure ZrN. Adding this information with references in literature [45,46], it can be estimated that solubility limit of Si in ZrN lattice is 2 at.%.

Table 3 also shows volumetric fraction of silicon nitride in Zr-Si-N thin films, as well as its coverage surface. It is noted that sample ZrSiN12.4 possess a Si_3N_4 volumetric fraction superior to 50.0%. The thickness of amorphous layer embedding ZrN grains is directly proportional to coverage surface value. When this parameter is equal or superior to 1, it is suggested that ZrN grains are completely embedded by Si_3N_4 amorphous layer [18,20].

Sample ZrSiN2.8 possess a relatively low coverage surface, which indicates that grains are not completely covered by amorphous layer, mainly due to the fact of, in this case, silicon concentration is near its solubility limit in ZrN matrix.

Furthermore, samples ZrSiN5.0, ZrSiN7.3 e ZrSiN10.0 show a coverage surface value near 1, indicating that, concerning nanostructure formation, segregation process was effective. Nonetheless, it is observed for sample ZrSiN12.4 a significant reduction in coverage surface value, which can be attributed to the drastic reduction of crystallite size (3 nm). In that case, boundaries areas are excessively increased, reducing the thickness of amorphous phase that separate crystal grains, even with the increase of Si_3N_4 volumetric fraction.

3.3. XPS

XPS analyzes were performed and the core-level spectra of Zr 3d, Si 2p and N 1s regions acquired from ZrN, ZrSiN2.8 and ZrSiN14.9 samples are shown in Fig. 3a, b and c. Analyzes of XPS spectra for pure ZrN, and Zr-Si-N with lowest and highest Si content, additionally with other characterization techniques, allow a thorough investigation of chemical states of all samples. Although the use of C 1s to perform spectra calibration carry an inaccuracy [47–49] differential charging effects were not considered within the analyzed samples.

Fig. 3a shows the Zr 3d photoelectron regions, where the best fit after deconvolution yielded two doublets. The doublet with lower binding energy is attributed to Zr $3d_{5/2}$ and Zr $3d_{3/2}$ (179.4 eV and 181.8 eV) electrons of ZrN. The doublet component at binding energy at 181.6 and 184.0 eV were assigned to Zr−O−N oxynitrides. Similar results can be observed in previous works [50–52]. The oxygen presence is possibly derived from residual O_2 and H_2O in the deposition chamber as also seen by RBS analysis. No significant binding energy shift was observed as the Si concentration was increased.

The XPS spectra from Si 2p region is shown in Fig. 3b. For ZrSiN14.9 sample it is possible to verify three peaks at 102.2 eV, 101.3 eV and 98.9 eV, corresponding to Si−O−N, SiN bonds and free silicon, respectively, Comparable results were obtained elsewhere [50,53]. According to RBS results, there is a nitrogen deficiency trend for samples with high Si content, including sample ZrSiN14.9. That generates free Si in the structure, identified by XPS. Similar behavior was also reported earlier by Musil and collaborators [54]. Sample ZrSiN2.8 presents a high background noise spectra caused by low Si concentration in the coating and will not be showed.

The best fit from N 1 s region for ZrSiN2.8 and ZrSiN14.9 samples is showed in Fig. 3c, which yielded four peaks, identified as Zr−O−N (396.3 eV), Si_3N_4 bonds (397.1 eV), ZrN (397.8 eV), and Si−O−N oxynitride compounds (399.4 eV), corroborating with the XPS results obtained for Zr 3d and Si 2p regions. As occurred at Zr 3d region, no significant BE shift was observed comparing samples ZrSiN2.8 and ZrSiN14.9 in N 1s region.

3.4. Instrumented indentation test

Fig. 4 shows the results of nanohardness tests for samples ZrN and Zr-Si-N. The hardness value for pure ZrN was 15.6 GPa, consistent with literature [26,31]. It is possible to observe that hardness values for samples ZrN, ZrSiN2.8, ZrSiN5.0 and ZrSiN7.3 are nearly the same, indicating that silicon addition up to 7.3 at.% is not sufficient to alter ZrN hardness values, or that substitutional solid solution formed in that stage does not contribute expressively to enhance hardness in that material.

On the other hand, from sample ZrSiN10.0 it is noted a hardness growth tendency, reaching a maximum of 20.6 GPa in sample ZrSiN14.9, which represents an enhancement of 32% when compared to pure ZrN.

Hardness increment with silicon addition is most certainly caused by the reduction of crystallite sizes and increase of residual tension in the films due to Si_3N_4segregation to grain boundaries. For crystal structures with crystallite sizes in the order of 10 nm, case of high content Si films, the main deformation mechanism is boundaries sliding. That process is highly restricted due to the formation of strong interface between crystal and amorphous phases, which results in an increase of residual tension levels and greater resistance to plastic deformation, finally manifested in the increase of hardness values.

It is also noted an increasing trend for H^3/E^2 ratio as Si content is raised. Such ratio is related to good performance against wear [55–57]. The sample ZrSiN14.9 presented the maximum value of 0.40 GPa, while TiN thin film, which is commonly applied as protective coating for wear, present values of 0.09 GPa to 0.15 GPa [58,59]. Therefore, silicon addition possibly causes the increment of wear resistance as well.

3.5. Oxidation behavior

Fig. 5a shows GAXRD patterns of ZrN sample before and after oxidation tests. After exposure to 773 K, there are still traces of the peak related to (111) plane, which disappear entirely at 873 K. Peak shift to the right occurs due to reduction in residual stress levels, promoted by increase in the mobility of atoms in such conditions. The peaks present in those patterns after oxidation tests are associated to monoclinic (M) and tetragonal (T) phases of zirconium oxide (ZrO_2), which indicates that at 773 K the film is already significantly compromised due to

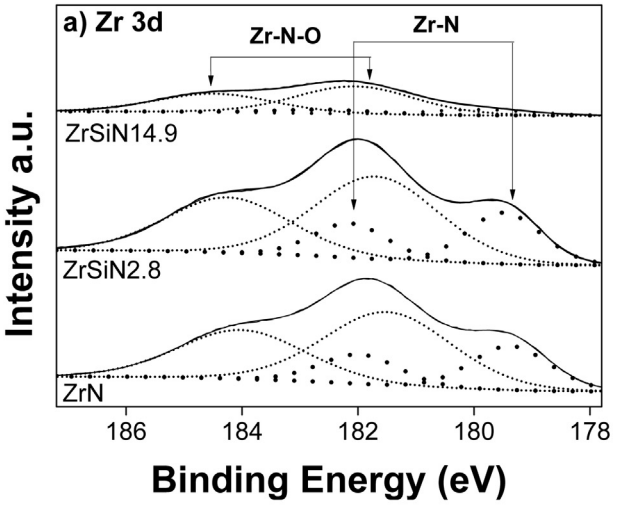

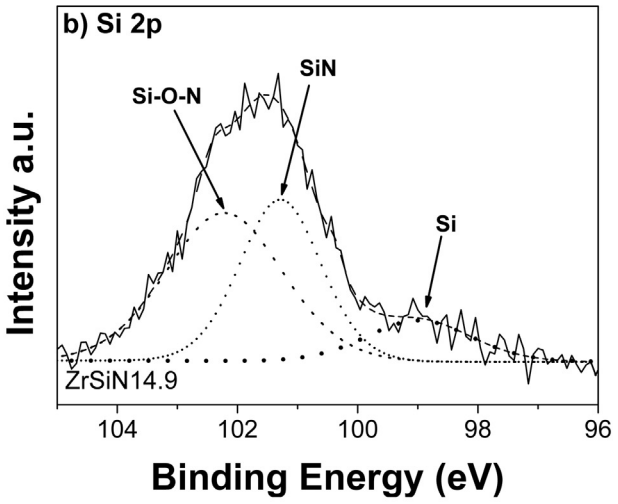

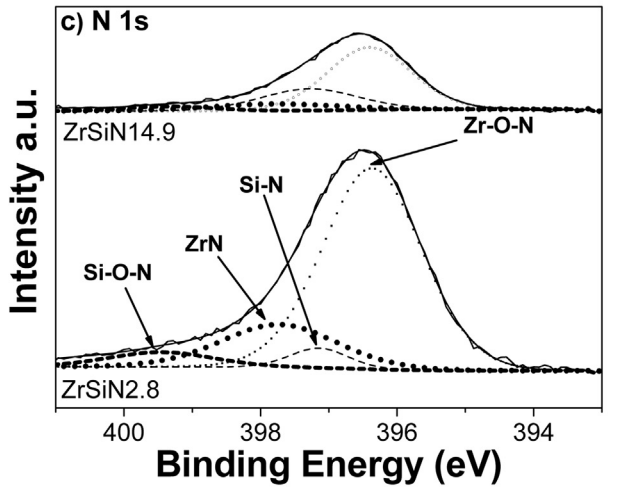

Fig. 3. X-ray photoelectron spectroscopy regions for (a) Zr 3d, (b) Si 2p, (c) N 1 s. The components used in the simulations are indicated in the figures.

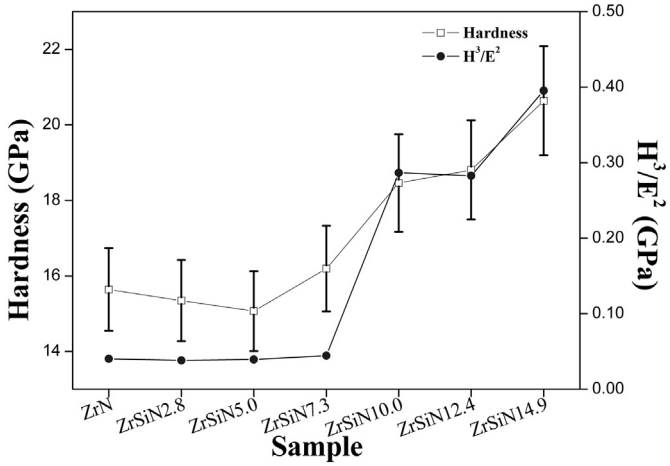

Fig. 4. Nanohardness and H^3/E^2results for ZrN and Zr-Si-N films.

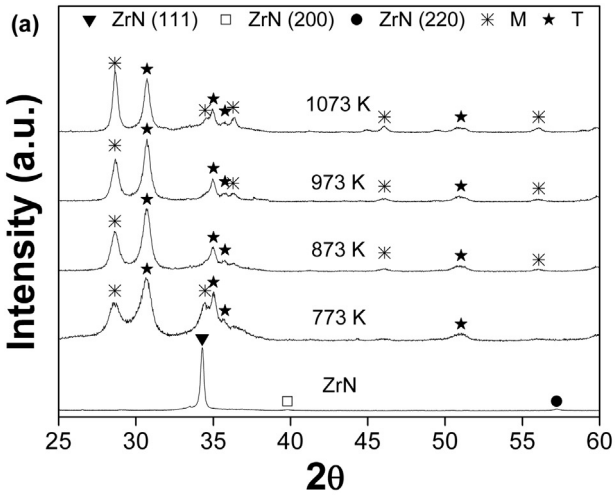

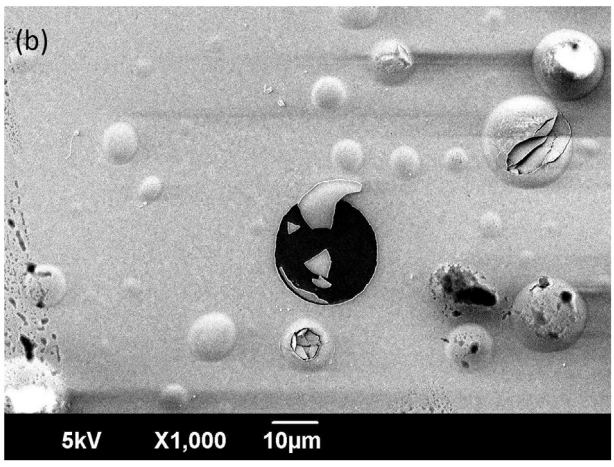

Fig. 5. (a) GAXRD analysis for sample ZrN subjected to oxidation tests at temperatures of 773 K to 1073 K. T indicates the tetragonal ZrO_2 phase, while M the monoclinic ZrO_2phase. (b) SEM analysis for sample ZrN after oxidation at 773 K. Film degraded by the decomposition process of nitrogen, which is responsible for the formation of surface bubbles.

oxidation.

Given that tetragonal phase of zirconium oxide is only stable at 1393 K or above, monoclinic phase ought to have been predominant after exposure to 773 K. However, it is known that it is possible to stabilize tetragonal zirconia in temperatures below 1373 K, provided that crystallites are nanometric in size [30]. Tetragonal phase possesses a lower surface energy than monoclinic one, thus, when crystallites are too small, the system tends to stabilize tetragonal zirconia in an attempt to minimize surface energy. Hence, it is noted that crystallite size of 36 nm is sufficiently small to promote stabilization of ZrO_2 at low temperatures.

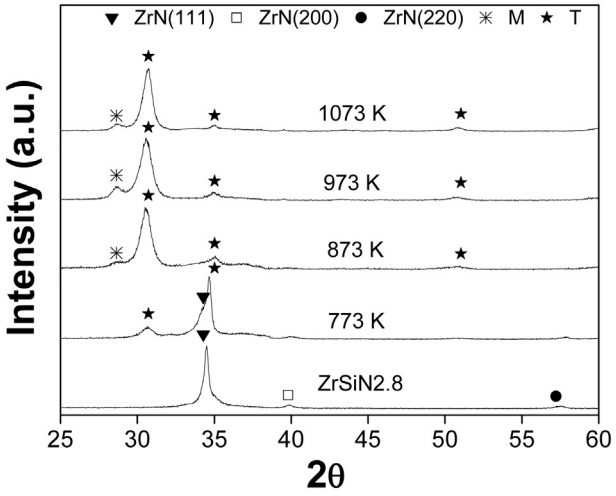

Fig. 6. GAXRD analysis for sample ZrSiN2.8 before and after oxidation tests at temperatures of 773 K to 1073 K.

Above 873 K only phenomena associated to loss of intensity of tetragonal phase related peaks and increase of intensity of monoclinic phase ones are observed.

Fig. 5b shows surface micrography of ZrN sample exposed to 773 K. Considerable degree of bubbles is observed, responsible for degradation of the film and exposure of the substrate to oxidizing atmosphere. Such bubbles are resultant of nitrogen decomposition process, which results in gaseous N_2 molecules that accumulate inside the lattice and provides the degradation of the film. Furthermore, free Zr atoms derived from that process, react with oxygen to form ZrO_2.

According to those results, nitrogen decomposition process starts in temperatures as low as 773 K, thus, characterizing its limited oxidation resistance.

Likewise, Si_3N_4 samples were subjected to oxidation tests. Results demonstrate that the film is still completely amorphous, even at 1373 K. Hence, exposure to high temperature of those films was not sufficient to crystallize Si_3N_4 phase nor form crystalline oxides.

Fig. 6 presents GAXRD patterns for samples ZrSiN2.8 before and after oxidation tests. Although peaks related to tetragonal ZrO_2 can be identified, peaks associated to plane (111) of ZrN are still strongly present. Such behavior indicates an improvement of oxidation resistance when compared to ZrN sample. On the other hand, no traces of ZrN peaks are observed at 873 K or above, where only phase transition of ZrO_2 from tetragonal to monoclinic can be identified. SEM analysis of sample ZrSiN2.8 (not showed) presents an identical behavior of pure ZrN, with bubbles rising at 773.

XRD patterns for sample ZrSiN5.0 before and after oxidation tests are shown in Fig. 7a, demonstrating a significant improvement in oxidation resistance when compared to the previously analyzed sample. It is possible to note that patterns obtained after exposure to 773 K are identical to those of as deposited sample. Furthermore, peaks related to ZrN are still present at 873 K.

Until 873 K no peaks associated to oxides are identified, however, peaks related to intermetallic $ZrSi_2$ formation are observed. That fact is probably associated to nitrogen decomposition process. At 973 K it is not possible to detect ZrN presence in the film. On the other hand, the film is not oxidized since identified peaks are associated to traces of tetragonal zirconia. Thus, at this point the structure is formed by intermetallic $ZrSi_2$ and amorphous silicon compounds.

The formation of such structure is attributed to the fact that, due to the presence of Si_3N_4 layer, diffusion of oxygen atoms is greatly restricted and free Zr atoms resultant from progressive nitrogen decomposition are unable to react with it. Zr atoms, then, eventually react with Si atoms resulting in $ZrSi_2$ formation. At 1073 K the film is

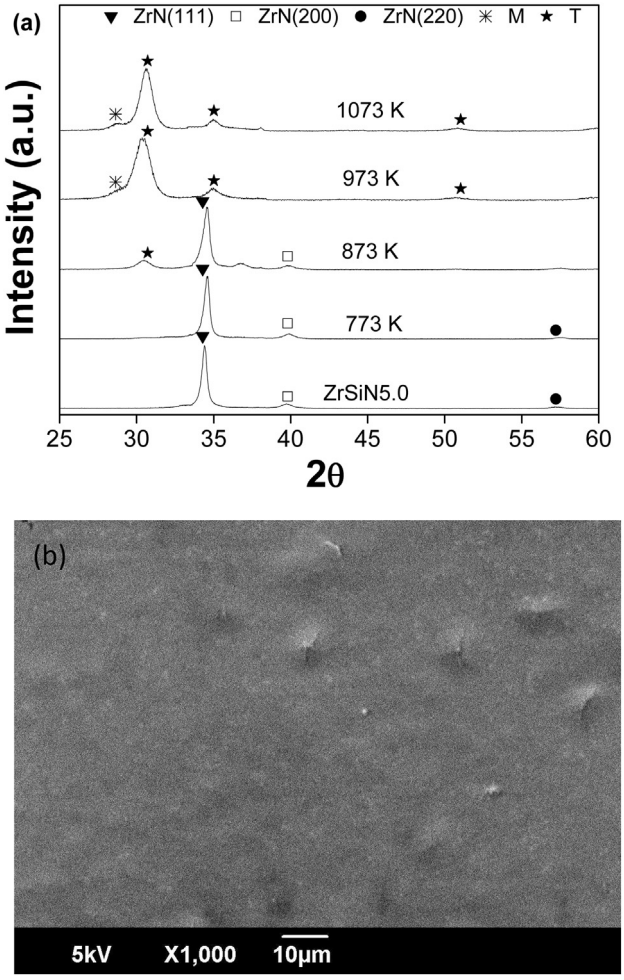

Fig. 7. (a) GAXRD analysis for sample ZrSiN5.0 subjected to oxidation tests at temperatures of 773 K to 1073 K. (b) SEM analysis for sample ZrSiN5.0 after oxidation at 973 K.

completely oxidized to tetragonal ZrO_2 and no $ZrSi_2$ related peaks can be detected.

Although nitrogen decomposition process apparently initiate at 873 K, no superficial imperfections are observed on ZrSiN5.0 samples. Defects derived from decomposition are only noticeable from 973 K, as shown in Fig. 7b with the formation of bubbles in the film surface.

Fig. 8a and b present GAXRD patterns for samples ZrSiN7.3 and ZrSiN10.0, respectively. At 873 K and 973 K, it is noted a trend for ZrN related peaks intensity reduction and an increase of intensity in $ZrSi_2$ related peaks. That fact suggests the increment of $ZrSi_2$ volumetric fraction as Si content is raised.

Fig. 9a shows GAXRD patterns for sample ZrSiN12.4 before and after oxidation tests. It is possible to verify that the behavior of this sample until 873 K is similar to the one registered to ZrSiN10.0. However, peaks associated to ZrN at 973 K can be identified. Thus, given that ZrN sample does not resist temperatures as low as 773 K, ZrSiN12.4 sample maintain ZrN grains stable up until 973 K. Hence, such concentration of silicon (12.4 at.%) is directly responsible for the increment of ZrN oxidation resistance in 200 K. Lastly, at 1073 K only peaks related to tetragonal ZrO_2 can be identified, so the sample is completely oxidized.

Finally, Fig. 9b shows GAXRD patterns for samples ZrSiN14.9 when subjected to oxidation tests, where it can be noted only the peak associated to plane (111) of ZrN, as deposited and when exposed to 773 K. Increase in temperature causes only a modification in intensity and broadening of peaks, when compared to sample ZrSiN12.4, preserving

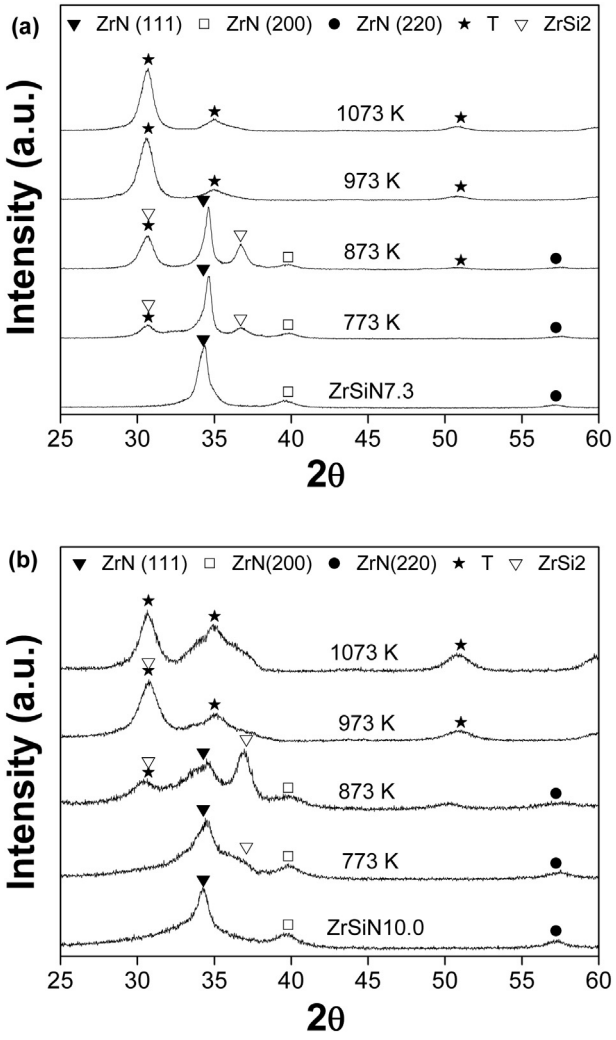

Fig. 8. GAXRD patterns for samples (a) ZrSiN7.3 and (b) ZrSiN10.0 subjected to oxidation tests at temperatures of 773 K to 1073 K.

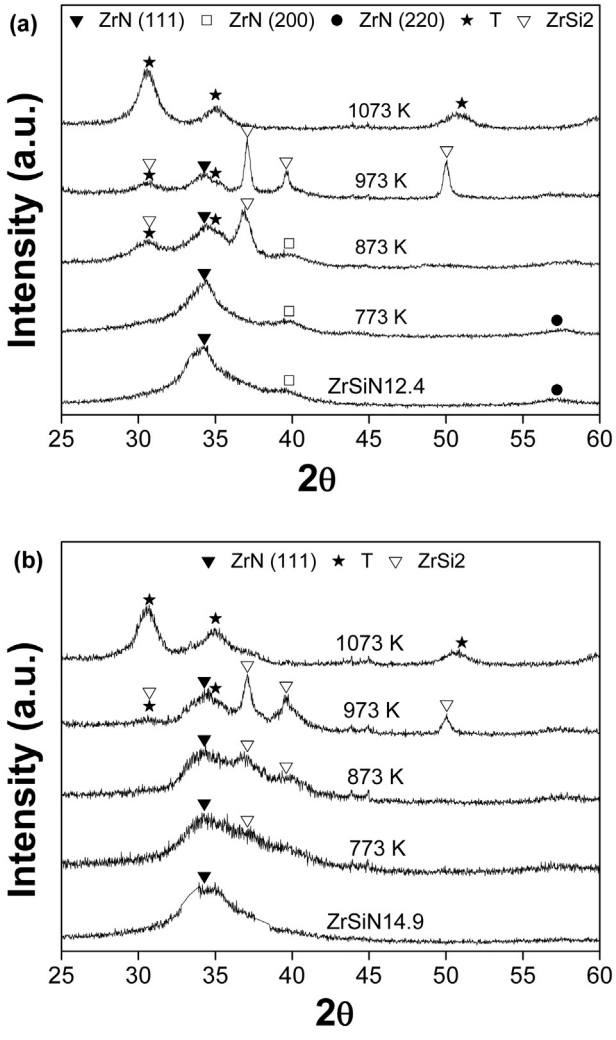

Fig. 9. GAXRD patterns for samples (a) ZrSiN12.4 and (b) ZrSiN14.9 subjected to oxidation tests at temperatures of 773 K to 1073 K.

the increment of oxidation temperature in at least 200 K. SEM analysis for samples ZrSiN7.3, ZrSiN10.0, ZrSiN12.4 and ZrSiN14.9 don't show bubbles in 1073 K, presenting the same behavior found in deposited coatings prior oxidation tests, proving the beneficial effect of silicon addition in oxidation resistance of the ZrN coatings.

4. Conclusions

In this work, microstructure, oxidation resistance and nanohardness properties of Zr-Si-N thin films were analyzed.

By GAXRD, all Zr-Si-N films present peaks related to pure ZrN, however, increasing the silicon concentration in coatings, it was observed loss of intensity and broadening of those peaks, with Si addition promoting the transition from a crystalline to an amorphous structure. Silicon addition also promotes a change in preferential orientation index from (111) to (200) to Zr-Si-N coatings.

XPS analyses suggests the presence of ZrN and Si_3N_4 composition for all Zr-Si-N samples, including sample ZrSiN2.8.

Silicon addition to ZrN films was responsible for significant increments in mechanical properties, with an increment in hardness values of 32%. Sample ZrSiN14.9 present the highest H^3/E^2 ratio, considerably superior when compared to showed in earlier works for TiN coatings, proving the potential of Zr-Si-N to be used in wear applications.

Sample ZrSiN2.8 does not show any modification in temperature of initiation and conclusion of decomposition and oxidation, when compared to ZrN sample. Samples ZrSiN12.4 and ZrSiN14.9 present 200 K increment of oxidation temperature in comparison to pure ZrN coating.

Acknowledgement

The authors thank CNPq, CAPES and FAPITEC/SE for financial support.

References

[1] S. Veprek, M.J.G. Veprek-Heijman, Industrial applications of superhard nanocomposite coatings, Surf. Coat. Technol. 202 (2008) 5063–5073, https://doi.org/10.1016/j.surfcoat.2008.05.038.

[2] V.K.W. Grips, V. EzhilSelvi, H.C. Barshilia, K.S. Rajam, Effect of electroless nickel interlayer on the electrochemical behavior of single layer CrN, TiN, TiAlN coatings and nanolayered TiAlN/CrN multilayer coatings prepared by reactive dc magnetron sputtering, Electrochim. Acta 51 (2006) 3461–3468, https://doi.org/10.1016/j.electacta.2005.09.042.

[3] V.K.W. Grips, H.C. Barshilia, V.E. Selvi, K.S. Rajam Kalavati, Electrochemical behavior of single layer CrN, TiN, TiAlN coatings and nanolayered TiAlN/CrN multilayer coatings prepared by reactive direct current magnetron sputtering, Thin Solid Films 514 (2006) 204–211, https://doi.org/10.1016/j.tsf.2006.03.008.

[4] L. Cunha, M. Andritschky, L. Rebouta, K. Pischow, Corrosion of CrN and TiAlN coatings in chloride-containing atmospheres, Surf. Coat. Technol. 116–119 (1999) 1152–1160, https://doi.org/10.1016/S0257-8972(99)00270-4.

[5] Y.H. Yoo, D.P. Le, J.G. Kim, S.K. Kim, P. Van Vinh, Corrosion behavior of TiN, TiAlN, TiAlSiN thin films deposited on tool steel in the 3.5 wt.% NaCl solution, Thin Solid Films 516 (2008) 3544–3548, https://doi.org/10.1016/j.tsf.2007.08.069.

[6] X.Z. Ding, A.L.K. Tan, X.T. Zeng, C. Wang, T. Yue, C.Q. Sun, Corrosion resistance of CrAlN and TiAlN coatings deposited by lateral rotating cathode arc, Thin Solid Films 516 (2008) 5716–5720, https://doi.org/10.1016/j.tsf.2007.07.069.

[7] G. Abadias, A. Michel, C. Tromas, C. Jaouen, S.N. Dub, Stress, interfacial effects and mechanical properties of nanoscale multilayered coatings, Surf. Coat. Technol. 202 (2007) 844–853, https://doi.org/10.1016/j.surfcoat.2007.05.068.

[8] J.K. Lee, G.S. Yang, Preparation of TiAlN/ZrN and TiCrN/ZrN multilayers by RF magnetron sputtering, Trans. Nonferrous Met. Soc. Chin. (2009) 795–799, https://doi.org/10.1016/S1003-6326(08)60352-0 (English Ed. 19).

[9] L. Van Leaven, M.N. Alias, R. Brown, Corrosion behavior of ion plated and implanted films, Corrosion 53 (1992) 25–34.

[10] R.M. Souto, H. Alanyali, Electrochemical characteristics of steel coated with TiN and TiA1N coatings, Corros. Sci. 42 (2000) 2201–2211, https://doi.org/10.1016/S0010-938X(00)00057-3.

[11] H. Barshilia, Corrosion behavior of nanolayered TiN/NbN multilayer coatings prepared by reactive direct current magnetron sputtering process, Thin Solid Films 460 (2004) 133–142, https://doi.org/10.1016/j.tsf.2004.01.096.

[12] S. Veprek, M.G.J. Veprek-Heijman, P. Karvankova, J. Prochazka, Different approaches to superhard coatings and nanocomposites, Thin Solid Films 476 (2005) 1–29, https://doi.org/10.1016/j.tsf.2004.10.053.

[13] J. Procházka, P. Karvánková, M.G.J. Vepřek-Heijman, S. Vepřek, Conditions required for achieving superhardness of ≥45 GPa in nc-TiN/a-Si3N4 nanocomposites, Mater. Sci. Eng. A 384 (2004) 102–116, https://doi.org/10.1016/j.msea.2004.05.046.

[14] S. Veprek, H.D. Männling, P. Karvankova, J. Prochazka, The issue of the reproducibility of deposition of superhard nanocomposites with hardness of ≥50 GPa, Surf. Coat. Technol. 200 (2006) 3876–3885, https://doi.org/10.1016/j.surfcoat.2004.11.023.

[15] S. Ma, J. Procházka, P. Karvánková, Q. Ma, X. Niu, X. Wang, D. Ma, K. Xu, S. Vepřek, Comparative study of the tribological behaviour of superhard nanocomposite coatings nc-TiN/a-Si3N4with TiN, Surf. Coat. Technol. 194 (2005) 143–148, https://doi.org/10.1016/j.surfcoat.2004.05.007.

[16] T. Zehnder, M. Diserens, Structure – performance relations in nanocomposite coatings, Surf. Coat. Technol. 147 (2001) 201–208, https://doi.org/10.1016/S0257-8972(01)01389-5.

[17] C.S. Sandu, S. Harada, R. Sanjinés, A. Cavaleiro, A unique approach to reveal the nanocomposite nc-MN/SiN-layer architecture of thin films via electrical measurements, Surf. Coat. Technol. 204 (2010) 1907–1913, https://doi.org/10.1016/j.surfcoat.2009.11.045.

[18] C.S. Sandu, R. Sanjinés, M. Benkahoul, F. Medjani, F. Lévy, Formation of composite ternary nitride thin films by magnetron sputtering co-deposition, Surf. Coat. Technol. 201 (2006) 4083–4089, https://doi.org/10.1016/j.surfcoat.2006.08.100.

[19] C.S. Sandu, R. Sanjinés, F. Medjani, Control of morphology (ZrN crystallite size and SiNxlayer thickness) in Zr-Si-N nanocomposite thin films, Surf. Coat. Technol. 202 (2008) 2278–2281, https://doi.org/10.1016/j.surfcoat.2007.09.003.

[20] C.S. Sandu, F. Medjani, R. Sanjinés, Optical and electrical properties of sputtered Zr-Si-N thin films: from solid solution to nanocomposite, Rev. Adv. Mater. Sci. 15 (2007) 173–178, https://doi.org/10.1016/j.surfcoat.2006.08.002.

[21] C.S. Sandu, M. Benkahoul, R. Sanjinés, F. Lévy, Model for the evolution of Nb-Si-N thin films as a function of Si content relating the nanostructure to electrical and mechanical properties, Surf. Coat. Technol. 201 (2006) 2897–2903, https://doi.org/10.1016/j.surfcoat.2006.06.003.

[22] C.S. Sandu, N. Cusnir, D. Oezer, R. Sanjinés, J. Patscheider, Influence of bias voltage on the microstructure and physical properties of magnetron sputtered Zr-Si-N nanocomposite thin films, Surf. Coat. Technol. 204 (2009) 969–972, https://doi.org/10.1016/j.surfcoat.2009.06.042.

[23] J. Musil, Hard nanocomposite coatings: thermal stability, oxidation resistance and toughness, Surf. Coat. Technol. 207 (2012) 50–65, https://doi.org/10.1016/j.surfcoat.2012.05.073.

[24] M. Benkahoul, C.S. Sandu, N. Tabet, M. Parlinska-Wojtan, A. Karimi, F. Lévy, Effect of Si incorporation on the properties of niobium nitride films deposited by DC reactive magnetron sputtering, Surf. Coat. Technol. 188–189 (2004) 435–439, https://doi.org/10.1016/j.surfcoat.2004.08.048.

[25] J. Lin, B. Wang, Y. Ou, W.D. Sproul, I. Dahan, J.J. Moore, Surface & coatings technology structure and properties of CrSiN nanocomposite coatings deposited by hybrid modulated pulsed power and pulsed dc magnetron sputtering, Surf. Coat. Technol. 216 (2013) 251–258, https://doi.org/10.1016/j.surfcoat.2012.11.053.

[26] J. Musil, R. Daniel, P. Zeman, O. Takai, Structure and properties of magnetron sputtered Zr-Si-N films with a high (≥25 at.%) Si content, Thin Solid Films 478 (2005) 238–247, https://doi.org/10.1016/j.tsf.2004.11.190.

[27] N. Ghafoor, I. Petrov, D.O. Klenov, B. Freitag, J. Jensen, J.E. Greene, ScienceDirect self-organized anisotropic (Zr 1 − x Si x) N y nanocomposites grown by reactive sputter deposition, Acta Mater. 82 (2015) 179–189, https://doi.org/10.1016/j.actamat.2014.09.029.

[28] J. Xu, H. Ju, L. Yu, Influence of silicon content on the microstructure, mechanical and tribological properties of magnetron sputtered Ti-Mo-Si-N films, Vacuum 110 (2014) 47–53, https://doi.org/10.1016/j.vacuum.2014.08.010.

[29] D. Pilloud, J.F. Pierson, A.P. Marques, A. Cavaleiro, Structural Changes in Zr–Si–N Films vs. Their Silicon Content, 181 (2004), pp. 352–356, https://doi.org/10.1016/j.surfcoat.2003.10.087.

[30] D. Pilloud, J.F. Pierson, M.C.M. De Lucas, M. Alnot, Stabilisation of tetragonal zirconia in oxidized Zr-Si-N nanocomposite coatings, Appl. Surf. Sci. 229 (2004) 132–139, https://doi.org/10.1016/j.apsusc.2004.01.048.

[31] J. Musil, Hard nanocomposite coatings: thermal stability, oxidation resistance and toughness, Surf. Coat. Technol. 207 (2012) 50–65, https://doi.org/10.1016/j.surfcoat.2012.05.073.

[32] G.B. Harris, Quantitative measurement of preferred orientation in rolled uranium bars, London, Edinburgh, Dublin, Philos. Mag. J. Sci. 43 (1952) 113–123, https://doi.org/10.1080/14786440108520972.

[33] C.K. Chung, H.C. Chang, S.C. Chang, M.W. Liao, Evolution of enhanced crystallinity and mechanical property of nanocomposite Ti-Si-N thin films using magnetron reactive co-sputtering, J. Alloys Compd. 537 (2012) 318–322, https://doi.org/10.1016/j.jallcom.2012.05.018.

[34] V.J. Trava-Airoldi, G. Capote, L.F. Bonetti, J. Fernandes, E. Blando, R. Hübler, P.A. Radi, L.V. Santos, E.J. Corat, J. Nanosci. Nanotechnol. 9 (6) (2009) 3891–3897, https://doi.org/10.1166/jnn.2009.NS85.

[35] R. Franz, M. Lechthaler, C. Polzer, C. Mitterer, Structure, mechanical properties and oxidation behaviour of arc-evaporated NbAlN hard coatings, Surf. Coat. Technol. 204 (2010) 2447–2453, https://doi.org/10.1016/j.surfcoat.2010.01.023.

[36] S. Hofmann, H.A. Jehn, Selective Oxidation and Chemical State of A1 and Ti in (Ti, Al) N, Coat. Surf. Interface Anal. 12 (1988) 329–333, https://doi.org/10.1002/sia.740120602.

[37] C.W. Kim, K.H. Kim, Anti-oxidation properties of TiAlN film prepared by plasma-assisted chemical vapor deposition and roles of Al, Thin Solid Films 307 (1997) 113–119, https://doi.org/10.1016/S0040-6090(97)00212-5.

[38] M. Benkahoul, E. Martinez, A. Karimi, R. Sanjinés, F. Lévy, Structural and mechanical properties of sputtered cubic and hexagonal NbNx thin films, Surf. Coat. Technol. 180–181 (2004) 178–183, https://doi.org/10.1016/j.surfcoat.2003.10.040.

[39] R. Lamni, E. Martinez, S. Springer, R. Sanjines, P. Schmid, F. Levy, Optical and electronic properties of magnetron sputtered ZrNx thin films, Thin Solid Films 447–448 (2004) 316–321, https://doi.org/10.1016/S0040-6090.

[40] X. Zhang, M.S. Byrne, R.J. Lad, Structure and optical properties of Zr1-xSixN thin films on sapphire, Thin Solid Films 518 (2009) 1522–1526, https://doi.org/10.1016/j.tsf.2009.09.025.

[41] S. Veprek, M.G.J. Veprek-Heijman, Limits to the preparation of superhard nanocomposites: impurities, deposition and annealing temperature, Thin Solid Films 522 (2012) 274–282, https://doi.org/10.1016/j.tsf.2012.08.048.

[42] M.A. Signore, A. Rizzo, L. Mirenghi, M.A. Tagliente, A. Cappello, Characterization of zirconium oxynitride films obtained by radio frequency magnetron reactive sputtering, Thin Solid Films 515 (2007) 6798–6804, https://doi.org/10.1016/j.tsf.2007.02.033.

[43] G. Abadias, Stress and preferred orientation in nitride-based PVD coatings, Surf. Coat. Technol. 202 (2008) 2223–2235, https://doi.org/10.1016/j.surfcoat.2007.08.029.

[44] R. Banerjee, R. Chandra, P. Ayyub, Influence of the sputtering gas on the preferred orientation of nanocrystalline titanium nitride thin films, Thin Solid Films 405 (2002) 64–72, https://doi.org/10.1016/S0040-6090(01)01705-9.

[45] M. Arab Pour Yazdi, F. Lomello, J. Wang, F. Sanchette, Z. Dong, T. White, Y. Wouters, F. Schuster, A. Billard, Properties of TiSiN coatings deposited by hybrid HiPIMS and pulsed-DC magnetron co-sputtering, Vacuum 109 (2014) 43–51, https://doi.org/10.1016/j.vacuum.2014.06.023.

[46] T. Schmitt, P. Steyer, J. Fontaine, N. Mary, C. Esnouf, M.O. Sullivan, F. Sanchette, Cathodic arc deposited (Cr, Si x) N coatings: from solid solution to nanocomposite structure, Surf. Coat. Technol. 213 (2012) 117–125.

[47] G. Greczynski, L. Hultman, Reliable determination of chemical state in x-ray photoelectron spectroscopy based on sample-work-function referencing to adventitious carbon: resolving the myth of apparent constant binding energy of the C 1s peak, Appl. Surf. Sci. 451 (2018) 99–103, https://doi.org/10.1016/j.apsusc.2018.04.226.

[48] H.J. Freund, H. Gonska, H. Lohneiss, G. Hohlneicher, Charging and rotational dependence of line position, J. Electron Spectrosc. Relat. Phenom. 12 (1977) 425–434, https://doi.org/10.1016/0368-2048(77)85093-7.

[49] A. Rizzo, M.A. Signore, L. Mirenghi, L. Tapfer, E. Piscopiello, E. Salernitano, R. Giorgi, Sputtering deposition and characterization of zirconium nitride and oxynitride films, Thin Solid Films 520 (2012) 3532–3538, https://doi.org/10.1016/j.tsf.2012.01.005.

[50] A. Winkelmann, J.M. Cairney, M.J. Hoffmana, P.J. Martin, A. Bendavid, Zr–Si–N films fabricated using hybrid cathodic arc and chemical vapour deposition: structure vs. properties, Surf. Coat. Technol. 200 (2006) 4213–4219, https://doi.org/10.1016/j.surfcoat.2005.01.004.

[51] M. Matsuoka, S. Isotani, W. Sucasaire, N. Kuratani, K. Ogata, X-ray photoelectron spectroscopy analysis of zirconium nitride-like films prepared on Si(100) substrates by ion beam assisted deposition, Surf. Coat. Technol. 202 (2008) 3129–3135, https://doi.org/10.1016/j.surfcoat.2007.11.019.

[52] P.J. Martin, A. Bendavi, J.M. Cairney, M. Hoffman, Nanocomposite Ti–Si–N, Zr–Si–N, Ti–Al–Si–N, Ti–Al–V–Si–N thin film coatings deposited by vacuum arc deposition, Surf. Coat. Technol. 200 (2005) 2228–2235, https://doi.org/10.1016/j.surfcoat.2004.06.012.

[53] D. Pilloud, J.F. Pierson, A.P. Marques, A. Cavaleiro, Structural changes in Zr–Si–N films vs. their silicon content, Surf. Coat. Technol. 180–181 (2004) 352–356, https://doi.org/10.1016/j.surfcoat.2003.10.087.

[54] J. Musil, Hard and superhard nanocomposite coatings, Surf. Coat. Technol. (2000) 322–330, https://doi.org/10.1016/S0257-8972(99)00586-1.

[55] F. Lv, S.P. Wen, R.L. Zong, F. Zeng, Y. Gao, F. Pan, Nanoindentation study of amorphous-Co79Zr13Nb8/Cr multilayers, Surf. Coat. Technol. 202 (2008) 3239–3245, https://doi.org/10.1016/j.surfcoat.2007.11.028.

[56] J. Soldán, J. Musil, Structure and mechanical properties of DC magnetron sputtered TiC/Cu films, Vacuum 81 (2006) 531–538, https://doi.org/10.1016/j.vacuum.2006.07.013.

[57] S.M. Yang, Y.Y. Chang, D.Y. Lin, D.Y. Wang, W. Wu, Mechanical and tribological properties of multilayered TiSiN/CrN coatings synthesized by a cathodic arc deposition process, Surf. Coat. Technol. 202 (2008) 2176–2181, https://doi.org/10.

1016/j.surfcoat.2007.09.004.
[58] G. Strapasson, P.C. Badin, G.V. Soares, G. Machado, C.A. Figueroa, R. Hubler, A.L. Gasparin, I.J.R. Baumvol, C. Aguzzoli, E.K. Tentardini, Structure, composition, and mechanical characterization of dc sputtered TiN-MoS2nanocompositethinfilms, Surf. Coat. Technol. 205 (2011) 3810–3815, https://doi.org/10.1016/j.surfcoat.2011.01.044.
[59] H.O. Pierson, Handbook of Refractory Carbides and Nitrides: Properties, Characteristics, Processing and Applications, First ed., (1996) Westwood, New Jersey.